Molecular beam study of the $a\,^3\Sigma^+$ state of NaK up to the dissociation limit

I. Temelkov,[1,2] H. Knöckel,[1] A. Pashov,[2] and E. Tiemann[1,*]
[1]*Institut für Quantenoptik, Leibniz Universität Hannover, 30167 Hannover, Germany*
[2]*Department of Physics, Sofia University, 5 James Bourchier Boulevard, 1164 Sofia, Bulgaria*
(Received 19 December 2014; published 23 March 2015)

We provide spectroscopic data for the $a\,^3\Sigma^+$ state of the $^{23}Na^{39}K$ molecule. The experiment is done in an ultrasonic beam apparatus, starting from the ground state $X\,^1\Sigma^+$ and driving the population to the $a\,^3\Sigma^+$ state, using a Λ scheme with fixed pump and scanning dump laser. The signals are observed as dips of the total fluorescence. The intermediate level is chosen to be strongly perturbed by the $B\,^1\Pi/c\,^3\Sigma^+$ states mixing to overcome the singlet-triplet transfer prohibition. We observed highly resolved hyperfine spectra of various rovibrational levels of the $a\,^3\Sigma^+$ state from $v_a = 2$ up to the highest vibrational levels for rotational quantum numbers $N_a = 4,6,8$. By the typical experimental linewidth of 17 MHz, the vibrational dependence of the hyperfine splitting is clearly revealed for NaK. The absolute frequency measurements of the vibrational levels are used for improvement of the $a\,^3\Sigma^+$ potential curve and of the derived scattering length of all natural isotope combinations. Applying the Λ scheme in the reverse direction can provide a pathway for efficient transfer of ultracold $^{23}Na^{39}K$ molecules from the $Na(3s) + K(4s)$ asymptote to the lowest levels of the ground state. We show spectra that couple the absolute ground state $v_X = 0, J = 0$ with an appropriate intermediate state for direct realization of the reverse path. The refined theoretical model of the coupled excited states of the $Na(3s) + K(4p)$ asymptote allows predictions of efficient paths for $^{23}Na^{40}K$; one example is calculated.

DOI: 10.1103/PhysRevA.91.032512 PACS number(s): 33.20.−t, 31.50.−x, 34.50.−s, 33.15.Pw

I. INTRODUCTION

Over the past decade physicists have invested serious effort in the creation of gases of ultracold molecules. Compared to atoms, where the dipole-dipole interaction is weak, being provided by the atomic magnetic moments [1], diatomic molecules can have large permanent electric dipole moments, leading to strong long-range interactions with its spatial anisotropy. Additionally, molecules provide many internal degrees of freedom compared to atoms, which widens the scope for experiments of controlling quantum systems constructed by molecules. The diatomic heteronuclear alkali-metal molecules are expected as a developmental step, which still keeps the complexity of the theoretical description on an acceptable level.

The procedure for creating ultracold diatomic molecules often applies an ensemble of ultracold atoms and uses photoassociation with subsequent spontaneous decay to ground-state molecules or uses magnetoassociation forming Feshbach molecules and employing stimulated Raman adiabatic passage (STIRAP) [2] for transferring the weakly bound state close to the dissociation limit to the desired bound level of the molecular ground state. This last method uses coherent processes and thus keeps full control of the quantum states. It was successfully applied to bring $^{40}K^{87}Rb$ to its absolute ground state [3]. Other good candidates for preparing Feshbach molecules are, e.g., $^{87}Rb\,^{133}Cs$ [4], $^{6}Li\,^{133}Cs$ [5], and $^{23}Na^{40}K$ [6,7], for which Feshbach resonances are observed. Photoassociation connected with spontaneous decay is much simpler to apply, but needs careful selection of the excitation for an efficient decay to the desired quantum state. It was demonstrated for LiCs [8], RbCs [9–11], NaCs [12], and KRb [13]. For both procedures a fairly deep knowledge of the electronic states is advantageous, mostly obtained by molecular spectroscopy with guidance of *ab initio* calculations.

As a simple rule, the requirements for observing long-range interactions in an ultracold gas are large dipole moment, low temperature, and high molecular density [3]. For alkali-metal dimers in the electronic ground state, LiCs has the largest permanent electric dipole moment of 5.5 D [14,15] decreasing to 2.72 D for NaK [16], 1.3 D for RbCs [17], and only 0.57 D for KRb [3]. Zuchowski and Hutson [18] discuss the selection of the most appropriate molecule ensemble from the point of view of chemical stability. Here KRb is unstable, with an exothermic reaction path to K_2 and Rb_2 requiring extra effort to obtain a sufficiently long observation time of such ensembles [19], whereas NaK is stable at ultralow temperatures in its absolute ground state. Even though LiCs has the largest dipole moment, the Cs nuclear spin $i_{Cs} = 7/2$ leads to long computing times modeling the LiCs molecule and LiCs is also unstable like KRb mentioned above. These considerations suggest that NaK would be a good compromise, providing a large permanent dipole moment, chemical stability, and simpler theoretical model selecting isotopes with low nuclear spins. Various groups are presently working on the creation of ultracold NaK. We recently analyzed possible transfer paths by Λ-type schemes in NaK, putting the focus on paths using nonresonant singlet-triplet coupling in the upper electronic states [20].

While NaK is one of the most explored alkali-metal dimers, high-precision *ab initio* calculations [21] and spectroscopic data for a number of electronic states are available. The ground state $X\,^1\Sigma^+$ and the lowest triplet state $a\,^3\Sigma^+$ are described by potential curves based on Fourier-transform spectroscopy of laser-induced fluorescence in a heat pipe [22]. Precise descriptions of the excited electronic states $A\,^1\Sigma^+$, $c\,^3\Sigma^+$, $B\,^1\Pi$, and $b\,^3\Pi$ are given in [23,24]. Sub-Doppler polarization spectroscopy in a heat pipe revealed the hyperfine structure (hfs) of the state $a\,^3\Sigma^+$[25]. However, there exists a significant gap between the highest observed vibrational

*Corresponding author: Tiemann@iqo.uni-hannover.de

levels of this state [22,26] and the asymptotic region where the Feshbach resonances take place. Also the hfs study in [25] does not provide sufficient resolution for exploring the expected vibrational dependence of the hyperfine coupling, which was already observed for other alkali-metal molecules such as Na_2 [27].

In our present work we put effort into providing spectra precise enough to quantify the vibrational dependence of the hyperfine structure of the state $a\,^3\Sigma^+$ and we study the rovibrational ladder starting from the tightly bound vibrational states up to the last existing rovibrational levels to improve the potential curve. Experimentally, we employ a Λ-type excitation scheme from $X\,^1\Sigma^+$ ($v_X = 0$) to a selected level v_a of $a\,^3\Sigma^+$, which is possible by resonant singlet-triplet coupling of the intermediate levels, showing that such schemes can be very efficient for existing mixing coefficients up to almost 50% [23]. We will discuss the inversion of such a process for producing ultracold molecules in the absolute ground state. Using our data we create a theoretical model for an accurate description of the hyperfine coupling of the state $a\,^3\Sigma^+$ and the spectra of the highest vibrational levels will provide the important information about the singlet-triplet mixing in the ground states $X\,^1\Sigma^+$ and $a\,^3\Sigma^+$.

II. EXPERIMENT

We investigated the NaK molecules in two laser fields to obtain precise data on the rovibrational energies including the hyperfine structure for the state $a\,^3\Sigma^+$. To overcome the singlet-triplet transition prohibition, we applied a Λ-type pump-dump scheme involving a strongly perturbed intermediate level, which is a mixture of the $B\,^1\Pi$ and $c\,^3\Sigma^+$ states. The potential scheme of the NaK molecule including the pump-dump steps is shown in Fig. 1. Starting with ground-state molecules, the fixed frequency pump laser couples a level of the molecular ground state with an excited level of the $B\,^1\Pi/c\,^3\Sigma^+$ system and creates fluorescence, which is monitored. The dump laser is tuned across the hyperfine transitions from the upper level to levels of the $a\,^3\Sigma^+$ state. When the dump laser hits a resonance, both the starting level and the final level are directly coupled and the fluorescence decreases.

NaK was created in a molecular beam; it is derived from a mixture of Na and K in natural isotopic abundance. The vacuum chamber for the apparatus had been constructed for a study of the Stark effect in NaK and detailed information can be found in [28]. A scheme of the whole setup is given in Fig. 2. The oven is a stainless steel container with a nozzle. It is filled with 30–40 g of Na and K with a mass ratio of 1:2 [29]. The working temperature of 830–880 K of the container is set by an external heater. The beam of molecules is formed by adiabatic expansion of the alkali-metal vapors through a 200-μm nozzle into a vacuum of 5×10^{-7} mbar and a skimmer 20 mm downstream of the nozzle, resulting in an averaged speed of 800 ± 100 m/s [28]. By the expansion, the NaK dimer is mainly in the lowest vibrational level $v_X = 0$ of the ground state $X\,^1\Sigma^+$ with small rotational energy. A 3-mm diaphragm placed 480 mm away from the nozzle ensures collimation of the beam and thus reduces the Doppler width by a factor of

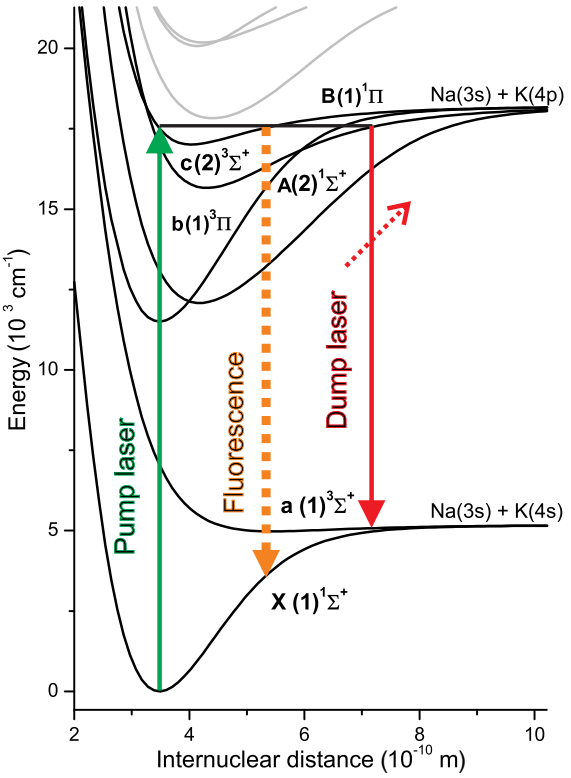

FIG. 1. (Color online) Potential scheme of NaK including the pump-dump steps. The pump laser connects an intermediate level of the $B\,^1\Pi$ state strongly coupled to the $c\,^3\Sigma^+$ state with the state $X\,^1\Sigma^+$. The dump laser connects the same intermediate level with various vibrational levels of the $a\,^3\Sigma^+$ state. The signals are observed as a dip in the fluorescence to the $X\,^1\Sigma^+$ state during a scan (tuning knob indicated by a small dashed arrow) of the dump laser when it crosses a $B\,^1\Pi/c\,^3\Sigma^+$-$a\,^3\Sigma^+$ resonance while the frequency of the pump laser is kept fixed.

320. It also separates the oven chamber and the chamber where the interaction with the laser beams takes place.

The molecular beam is crossed perpendicularly by two parallel running laser beams optimized for STIRAP coupling of the $X\,^1\Sigma^+$ and the $a\,^3\Sigma^+$ states. For the pump laser we employed a ring dye laser (Coherent CR-699) with rhodamine 6G, excited by an Ar^+ laser (Coherent Innova 400). For the dump transition we used a Ti:sapphire laser (Teknoscan TIS-SF-07) pumped by a frequency-doubled Nd:YAG laser (Coherent Verdi 10 W). Both pump and dump laser beams are focused and overlapped by cylindrical optics. The shapes of the laser beams in the interaction zone were prepared to be elliptical with the long axis perpendicular to the molecular beam with dimensions of 0.3×4 mm^2 for the Ti:sapphire laser and 0.3×7 mm^2 for the dye laser. The displacement between the laser beams could be varied in the direction of the molecular beam from 0.05 to 0.30 mm looking for the strongest possible drop of the fluorescence during a resonance. Both laser fields have linear polarization parallel to the molecular beam direction. The laser powers applied to the molecules in the chamber were 11–14 mW by the dye laser and 15–460 mW by the Ti:sapphire laser.

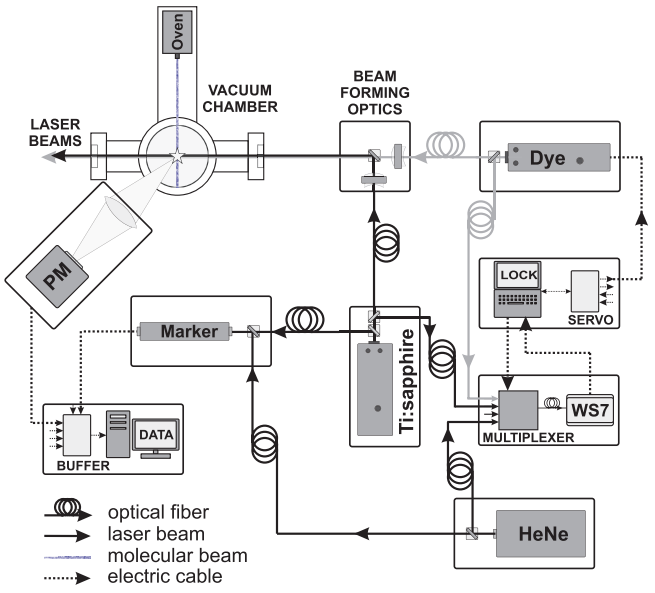

FIG. 2. (Color online) Simplified scheme of the experimental setup. The molecular beam is crossed perpendicularly by two laser beams from the dye and the Ti:sapphire laser running parallel, focused, and overlapped by the beam forming optics. The resulting fluorescence is observed by the photomultiplier (PM). The absolute frequencies of the two lasers, together with the reference HeNe laser, are monitored by the wavemeter WS7 via an optical multiplexer. The frequency of the dye laser is long-term stabilized by a servo system involving the wavemeter for setting the laser to the requested frequency. A confocal cavity gives relative frequency markers when the Ti:sapphire laser is tuned. The data are collected and recorded by the data acquisition system via a buffer box.

By a set of two short-pass filters (Balzers Optics Calflex X, cutoff wavelength 730 nm) and one long-pass filter (Schott OG590), the fluorescence frequency band is narrowed before reaching the photomultiplier. The filters suppress the scattered light coming from the laser beams, a part of the fluorescence to the singlet state, and the whole fluorescence to the $a\,^3\Sigma^+$ state. The laser stray light is additionally reduced by a series of conic apertures arranged along the laser beam path. The fluorescence light is imaged onto the photomultiplier (R943-02 in a Peltier cooled housing C4877-02 with a C4877 controller from Hamamatsu) by a spherical mirror mounted under and a lens placed above the interaction volume [30].

Laser frequencies were measured by a wavemeter (High Finesse WS7), which was calibrated regularly with a HeNe laser stabilized to an iodine hyperfine transition. The specified uncertainty of the WS7 is 100 MHz, but for several tests using diode lasers locked on precisely known transitions in rubidium we observed an absolute long-term precision of about 45 MHz corresponding to 0.0015 cm^{-1}. Both the pump and the dump lasers are short-term stabilized to low-finesse external interferometers, reducing their linewidths to 1–2 MHz. For the long-term frequency stabilization of the dye laser we use the readings of the WS7 and a small program that via a digital-to-analog converter board (Velleman K8061) keeps the dye laser at the chosen frequency to within a few MHz. The principle of our measurements requires a low level of power fluctuation in the pump field. We achieve this by employing a special low-turbulence nozzle (Radiant Dyes) in the dye laser. Additionally, a power noise suppressor (Thorlabs LCC3111) mounted close to the vacuum chamber keeps the power fluctuations below 3%.

For relative frequency measurements during the frequency scans of the Ti:sapphire laser, we use the markers of a confocal Fabry-Pérot interferometer with a free spectral range of 148.95 ± 0.07 MHz, which was locked to the iodine-stabilized HeNe laser. For collecting the data we use a PC with a data acquisition card (National Instruments PCI-6221). The system is controlled by a LABVIEW program providing simultaneous recording of up to eight signals. Typical acquisition intervals were set to 10 ms.

III. MEASUREMENTS

The interaction between the molecules and the pump laser is observed as fluorescence from the excited level to the ground-state vibrational manifold. When the dump laser is tuned across a resonance with a level of the $a\,^3\Sigma^+$ state, the fluorescence drops. For the discussion of the coupling in the intermediate state we use the total rotational angular momentum quantum number J as a good quantum number, as the coupling between the $B\,^1\Pi$ state and the $c\,^3\Sigma^+$ state is due to the spin-orbit interaction and is only indirectly influenced by the hyperfine interaction. The total angular momentum of levels of the $B\,^1\Pi$ state is denoted by J and their parity by $(-1)^{J+\epsilon}$, where ϵ is zero for e levels and 1 for f levels. The total angular momentum $\vec{J}$ in the $c\,^3\Sigma^+$ state is expressed as $\vec{J} = \vec{N} + \vec{S}$, where $\vec{N}$ and $\vec{S}$ are the rotational angular momentum and total electron spin with $S = 1$ here. Therefore, any rotational level N is split into three sublevels by the spin-rotation interaction, giving the levels $J = N + 1$, $J = N$, and $J = N - 1$. The parity of the levels is determined by $(-1)^N$. Only levels with the same J and parity of the $B\,^1\Pi$ state and the $c\,^3\Sigma^+$ state can couple. Considering only levels closest in energy, an e level of quantum number J of the $B\,^1\Pi$ state will couple to a level $(N = J, J)$ of the $c\,^3\Sigma^+$ state and an f level of the $B\,^1\Pi$ state will couple to levels $(N = J + 1, J)$ and $(N = J - 1, J)$ of the $c\,^3\Sigma^+$ state. So by pumping ${}^RQ(J_X)$ or $Q(J_X)$ transitions[1] with $J_X - J_B = \Delta J = 0$ from the $X\,^1\Sigma^+$ ground-state level $v_X = 0, J_X = 6$ to intermediate f levels $v_B = 8, J_B = 6$, which were employed mostly here, levels $N = 7, J_c = 6$ and $N = 5, J_c = 6$ and $v_c = 30$ of the $c\,^3\Sigma^+$ state are coupled [23]. The hyperfine splittings of ground-state levels and of $B\,^1\Pi$ levels are generally small, however, coupling of $B\,^1\Pi$ levels with $c\,^3\Sigma^+$ levels leads to an easily observable hyperfine splitting [23].

As examples for greater clarity we show laser excitation spectra of the two lines ${}^RQ(6)$ and $Q(6)$ of the $X\,^1\Sigma^+$ $(v_X = 0)$–$B\,^1\Pi$ $(v_B = 8)/c\,^3\Sigma^+$ $(v_c = 30)$ system in Fig. 3 (we use the vibrational numbering of the $c\,^3\Sigma^+$ state due to the recent work by Ferber *et al.* [24]). The $Q(6)$ transition shows almost the same hyperfine splitting as the ${}^RQ(6)$ one, indicating the strong mixing of the levels for $J_B = J_c = 6$ [23].

[1]The superscript R labels a transition with $\Delta N = 1$ for the basis vector where N is specified, i.e., the state $c\,^3\Sigma^+$, whereas the main symbol Q refers to $\Delta J = 0$ of the total angular momentum J.

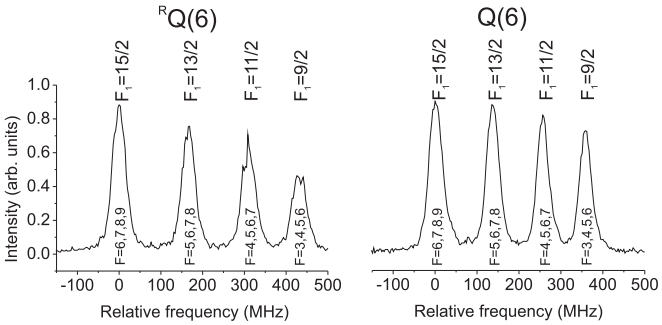

FIG. 3. Laser excitation spectra of the perturbed lines $^R Q(6)(8/30\text{–}0)$ and $Q(6)(8/30\text{–}0)$ of the $X\,^1\Sigma^+\text{–}B\,^1\Pi/c\,^3\Sigma^+$ band. The quartet structure is caused by the hyperfine structure of the ^{23}Na nucleus with sodium nuclear spin $i_{\mathrm{Na}} = 3/2$. Due to the coupling scheme $\vec{F}_1 = \vec{J} + \vec{i}_{\mathrm{Na}}$, intermediate quantum numbers $F_1 = 15/2,13/2,11/2,9/2$ are assigned to the lines of the quartet. The hyperfine splitting due to the coupling scheme $\vec{F} = \vec{F}_1 + \vec{i}_{\mathrm{K}}$ of the ^{39}K nucleus is not resolved.

The power of the pump laser is decreased until a reasonable compromise between a narrow linewidth and a sufficient signal-to-noise ratio (SNR) is achieved. Quartets appear due to the hyperfine interaction of the ^{23}Na nucleus with nuclear spin $i_{\mathrm{Na}} = 3/2$. The coupling scheme $\vec{F}_1 = \vec{J} + \vec{i}_{\mathrm{Na}}$ is appropriate because the hyperfine interaction by Na being mainly in the $3s$ state is larger than that by K in the $4p$ state. Thus intermediate quantum numbers $F_1 = 15/2,13/2,11/2,9/2$ are assigned to the lines of the quartet. Each of the lines of the quartet contains the hyperfine structure due to the coupling scheme $\vec{F} = \vec{F}_1 + \vec{i}_{\mathrm{K}}$ of the ^{39}K nucleus with $i_{\mathrm{K}} = 3/2$. This is not resolved in our spectra, but leads to additional broadening of each of the four components by about 5 MHz, as estimated from the known atomic hyperfine coupling of K in its $4p$ state [31].

For most of the measurements the $^R Q(6)$ line was employed as the pump transition and we can dump into levels with $N = 6$ and 8 of state $a\,^3\Sigma^+$. For a few measurements we selected the $^R Q(4)$ and the $Q(6)$ lines also from the B-X (8-0) band to check for internal consistency of the data. The main set of measurements was done by setting the pump laser on the component $F_1 = 15/2$ of the $^R Q(6)$ line with frequency $17\,451.9546 \pm 0.0015$ cm^{-1} determined by the wavemeter.

If we neglect the coupling of the $B\,^1\Pi$ state to the $c\,^3\Sigma^+$ state, the approximate lifetime for $v_B = 8$ of the $B\,^1\Pi$ state is about 16.5 ns [32], which corresponds to a natural width of 10 MHz. The residual Doppler broadening is expected to be 4.4 MHz due to the collimation ratio of 1/320 (full Doppler width of 1.4 GHz for a temperature of 860 K). From the convolution of the residual Doppler width, the natural linewidth, and the potassium splitting of 5 MHz of each component of the $^R Q(6)$ quartet, we expect a linewidth of 17 MHz. However, the narrowest linewidth of the pumping line observed in the case of negligible power broadening (pumping power of 0.25 mW and laser beam diameter of 3 mm) is 27 MHz. This significant broadening is not yet understood. To reach a sufficient SNR during the measurements we were forced to use higher pumping power, resulting in linewidths of up to 55 MHz.

A. Relative frequency measurements

For relative frequency measurements of the hyperfine structure of various vibrational levels of state $a\,^3\Sigma^+$, the pump laser was set on the resonance maximum to the intermediate level and the dump laser was tuned across the $B\,^1\Pi/c\,^3\Sigma^+\text{–}a\,^3\Sigma^+$ resonances. The initial guess of the dump frequencies for each vibrational level was obtained from former experiments in a heat pipe [22].

The achieved signal-to-noise ratio of only 4–5 in the best cases for the deepest dips of the strongest hyperfine lines was not sufficient for extracting spectra by a single scan of the dump laser. Therefore, we recorded several consecutive scans under the same physical conditions. Using the recorded peaks from the marker cavity for overlapping the spectra, the individual scans were averaged to reduce the statistical noise, reaching a SNR up to 65 for about 200 scans. Experimentally, we found that for a single scan, a frequency range of around 4–5 GHz tuned in 15–20 s gives optimal results. This scanning speed and the LABVIEW acquisition time set to 10 ms lead to a frequency step size of around 3 MHz in the recordings. The steps vary smoothly between 2.5 and 3.5 MHz along each scan, due to the nonlinearity of the piezoelements tuning the dump laser, but the recordings are linearized using the markers. Typical linewidths achieved in the hyperfine spectra of the state $a\,^3\Sigma^+$ were 17 MHz. During the tests we were able to observe linewidths down to 12 MHz by minimizing the pump and dump laser power, but then the SNR was not satisfactory.

For the state $a\,^3\Sigma^+$ both the sodium and potassium atoms have spherical s orbitals, therefore the spin-spin and the spin-orbit interactions are expected to be weaker than the Fermi contact interaction. Because the sodium hyperfine interaction is stronger than the one by potassium, the convenient coupling scheme is $\vec{G}_1 = \vec{S} + \vec{i}_{\mathrm{Na}}, \vec{G}_2 = \vec{G}_1 + \vec{i}_K$ and finally the rotation N couples to G_2 to give the total angular momentum F by $\vec{F} = \vec{G}_2 + \vec{N}$ [25].

In the case of $v_a = 5, N_a = 6$ of the state $a\,^3\Sigma^+$, we used also the $F_1 = 13/2,11/2,9/2$ components as intermediate levels. Having spectra via all the components of the $^R Q(6)$ quartet reveals all the hyperfine features of the $a\,^3\Sigma^+$ spectra that are not visible in spectra from the $F_1 = 15/2$ level due to the selection rules $\Delta F = F' - F = 0, \pm 1$, where F' and F are the total angular momenta of the upper and the lower state, respectively.

In Fig. 4 we give three examples of spectra by dumping to vibrational levels $v_a = 5,17,18$ and rotational angular momentum quantum number $N_a = 6$. At first glance one can see three clearly separated groups of lines with additional splitting within each group. In the case of $v_a = 5$, which is a deeply bound state, there is a significant substructure in the groups that almost vanishes for $v_a = 17$ and 18, whereas the overall splitting of the hfs is varying only little. The last vibrational level before the dissociation is $v_a = 18$ for a rotational state $N_a = 6$. There a radical change of the sequence of lines in the middle group is clearly visible compared with the $v_a = 17$ spectrum. The achieved resolution thus allows observation of a significant vibrational dependence of the hyperfine spectrum. This could not be observed in the investigations of the state $a\,^3\Sigma^+$ by Ishikawa [25].

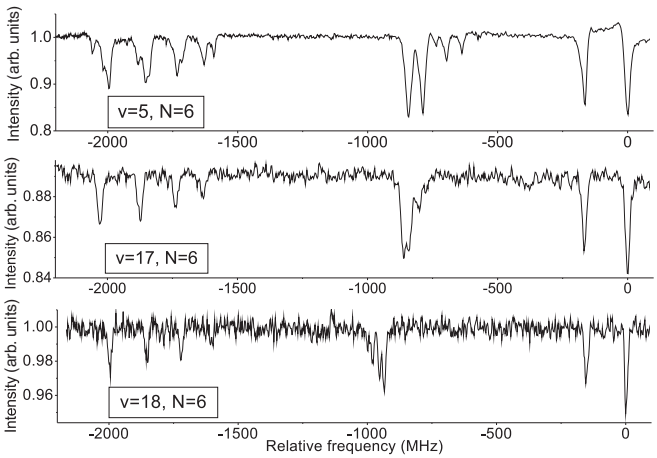

FIG. 4. Hyperfine structure of the state $a\,^3\Sigma^+$ for vibrational levels $v_a = 5,17,18$ and $N_a = 6$. The line $^RQ(6)$ with hyperfine component $F_1 = 15/2$ of the mixed levels $B\,^1\Pi$ ($v_B = 8, J_B = 6$)/ $c\,^3\Sigma^+$ ($v_c = 30, J_c = 6$) was pumped.

On some hyperfine components we observed specific profile asymmetry and fluorescence levels higher than the background level set by the pump laser. This is an indication of the nonlinearity of the STIRAP process projected on the $a\,^3\Sigma^+$ spectra. A full investigation of the STIRAP process is not the purpose of this work, therefore the employed experimental setup does not allow precise measurements of the power and beam profiles of the lasers in the zone of interaction with the NaK molecules. The laser powers were just kept as low as possible to minimize the nonlinear effects in order to avoid line shifts, keeping the SNR still high enough. The difference frequencies between the hyperfine components could be determined with an accuracy between 5 and 25 MHz with the help of the marker cavity.

B. Absolute frequency measurements

While maintaining the two-photon resonance, the absolute frequencies of the pump and the dump laser were simultaneously measured by the wavemeter. The dump frequency was set manually on a selected dip in the spectrum. We chose a sharp and strong feature of hyperfine transitions to the state $a\,^3\Sigma^+$, which was already recognizable without any averaging, usually the dip corresponding to the strongest of the doublet of lines on the high-frequency side of the hyperfine spectra (see Fig. 4).

When the reference resonance for a certain rovibrational level was found, we made 10–12 consecutive measurements within 3–4 min, collecting dump frequencies. Such a set shows a statistical uncertainty below 3 MHz. During this period the pump frequency is stabilized within a few MHz by the wavemeter. The reproducibility was checked by repeating several times such a measurement a few weeks later, which resulted in a statistical deviation of ±30 MHz over the whole set of measurements. The systematic uncertainty of the wavemeter is obtained to be ±45 MHz, derived by calibration with well-known iodine spectra.

When the angle between the laser beam and atomic beam deviates from 90°, a first-order Doppler shift appears. We chose both laser beams to have the same propagation direction in the volume of interaction with the molecules. Thus the signs of the Doppler shifts for the pump and dump laser are equal and the desired two-photon resonance frequency difference $\nu_\Delta = \nu_{\rm pump} - \nu_{\rm dump}$ becomes less sensitive to angle mismatch because of the small difference between $\nu_{\rm pump}$ and $\nu_{\rm dump}$. Actually, a residual Doppler shift contributes not more than 4 MHz to the frequency differences.

IV. THEORETICAL MODEL

For a quantitative description of the hyperfine interaction of the state $a\,^3\Sigma^+$ the full Hamiltonian of the ground-state system including state $X\,^1\Sigma^+$ can be written in the following form [33]:

$$H = T_n + U + H_{\rm hfs} + H_{\rm SS}, \tag{1}$$

where T_n is the kinetic energy of the relative motion of the two atoms. The atomic masses are taken from the tables in [34]. Here U is the potential energy

$$U = U_X(R)P_X + U_a(R)(1 - P_X), \tag{2}$$

where U_X and U_a are the potential energies of the states $X\,^1\Sigma^+$ and $a\,^3\Sigma^+$ as a function of the internuclear distance R and P_X and $1 - P_X$ are projection operators on the uncoupled states $X\,^1\Sigma^+$ and $a\,^3\Sigma^+$, respectively.

The hyperfine contribution $H_{\rm hfs}$ is determined mainly by the Fermi contact term of the interaction between the electron spins $\vec{s}_{\rm Na}$ and $\vec{s}_{\rm K}$ and the nuclear spins $\vec{i}_{\rm Na}$ and $\vec{i}_{\rm K}$,

$$H_{\rm hfs} = a_{\rm Na}(R)\vec{s}_{\rm Na}\vec{i}_{\rm Na} + a_{\rm K}(R)\vec{s}_{\rm K}\vec{i}_{\rm K}, \tag{3}$$

where $a_{\rm Na}$ and $a_{\rm K}$ are atomic Fermi contact terms for Na and K, respectively. The possible R dependence of the hyperfine parameters describes the distortion of the considered atom by the binding to the other one. The atomic magnetic hyperfine parameters are taken from [35] for $R \to \infty$. The term $H_{\rm SS}$ represents the spin-spin interaction

$$H_{\rm SS} = \tfrac{2}{3}\lambda(R)\left(3S_Z^2 - S^2\right), \tag{4}$$

where the parameter λ is a function proportional mainly to $1/R^3$ as the dipole-dipole interaction, but it contains also contributions from second-order spin-orbit interactions, and S_Z is the projection of the total electronic spin S on the molecular axis Z.

The calculations incorporate Born-Oppenheimer potentials according to Hund's coupling case b. Each representation of the potentials for the two states with the common atomic asymptote $3s + 4s$ is split into three regions of the internuclear separation R: a repulsive short-range region $U_{\rm SR}(R)$, an asymptotic long-range part $U_{\rm LR}(R)$, and the intermediate region $U(R)$ with the potential minimum. The analytic forms of the three regions of the R functions are given by the following formulas:

$$U_{\rm SR}(R) = A + \frac{B}{R^q} \quad \text{for} \quad R < R_i, \tag{5}$$

$$U(R) = \sum_{k=0}^{n} a_k x^k \quad \text{for} \quad R_i \leqslant R \leqslant R_o, \tag{6}$$

TABLE I. Map of the observed $a\,^3\Sigma^+$ rovibrational levels (v,N). The intermediate level is excited by the pump transition $^RQ(6)$ to the mixed state $B\,^1\Pi/c\,^3\Sigma^+$, $F_1 = 15/2$.

	v								
N	2	3	4	5	9	13	16	17	18
4				x					
6		x	x	x	x	x	x	x	x
8	x	x	x	x	x	x	x	x	

with $x = \frac{R-R_m}{R+bR_m}$, and

$$U_{\rm LR}(R) = -\frac{C_6}{R^6} - \frac{C_8}{R^8} - \frac{C_{10}}{R^{10}} \pm E_{\rm ex} \quad \text{for} \quad R > R_o. \tag{7}$$

Here A, B, and q are parameters, R_m is close to the internuclear distance of equilibrium, b is a parameter giving the function x a steeper slope for $R < R_m$ compared to the side $R > R_m$, a_k are polynomial coefficients, R_i and R_o denote the connection points between the three R regions, $C_{6,8,10}$ are the conventional dispersion coefficients, and $E_{\rm ex}$ is the exchange term expressed by

$$E_{\rm ex} = A_{\rm ex} R^{\gamma} e^{-\beta R}, \tag{8}$$

with a negative sign for the singlet and positive for the triplet state potential in Eq. (8). The coefficient C_6 is taken from [36], C_8 from [37], and C_{10} was used as a fitting parameter. The magnitude $A_{\rm ex}$ was varied keeping γ and β fixed as derived from ionization energies [38].

V. DATA EVALUATION

The set of the investigated rovibrational levels is given in Table I; Fig. 4 shows examples of spectra where the intermediate level was $F_1 = 15/2$ excited by the $^RQ(6)$ line. Some spectra were repeatedly recorded on different days to estimate the statistical uncertainty of the difference frequency between the hfs components. We found that it was always below 10 MHz.

In Fig. 5 a spectrum of $v_a = 5, N_a = 6$ of the state $a\,^3\Sigma^+$ with assigned quantum numbers G_1, G_2, and F is shown.

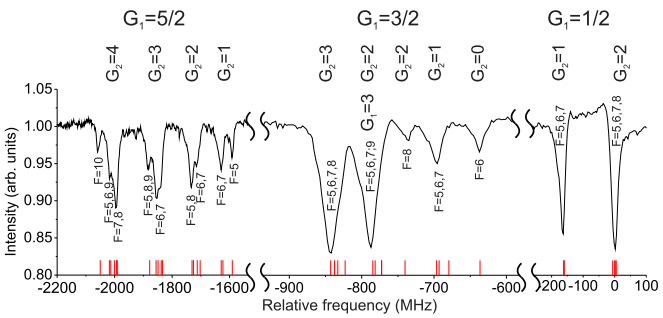

FIG. 5. (Color online) Comparison between the experimental and the calculated spectrum for $N_a = 6, v_a = 5$. The calculated frequency of each allowed hyperfine component is given as a red vertical bar at the bottom of the diagram. The intermediate level was $J_c = 6, F_1 = 15/2$.

The empty spectral spaces between the three groups are cut out from the picture, allowing higher magnification of the interesting regions. The three groups result from the coupling of the total electron spin $S = 1$ with the nuclear spin of Na giving $G_1 = 5/2, 3/2, 1/2$. Adding the K nuclear spin $i_{\rm K}$ gives G_2 for the lines in the subgroups for each G_1, which are also completely resolved. The weak coupling by effective spin-spin interaction leads to a manifold of the total angular momentum $\vec{F} = \vec{G}_2 + \vec{N}$, which is resolved only for a few cases and leads mostly to overlapping lines with asymmetric profiles. To prepare the fit we derived the frequency differences of all peaks with respect to the highest-frequency component $G_1 = 1/2$, $G_2 = 2$ for each v and estimated different uncertainties (from 5 to 25 MHz) depending on the SNR, on the overlap of components thus giving a broader line or for a line appearing as a shoulder on a strong one.

In one approach we tried to fit the hyperfine pattern of all observed vibrational levels by using the atomic data for the hyperfine interaction [35], i.e., the parameters in Eq. (3) were assumed to be independent of the internuclear separation R. However, we found a significant systematic trend in the deviations with smaller splittings than expected for low vibrational levels. Thus we have to define for each hyperfine interaction a function of R, which we choose very simply to be

$$a_i(R) = a_i^{\rm atom}\left(1 + \frac{b_i}{\exp[(R - R_{\rm hfs})/dR] + 1}\right), \tag{9}$$

where the subscript i stands for Na or K and the second term in large parentheses represents a monotonically decreasing function with increasing R. The total expression goes asymptotically to the atomic amplitude and we expect for b_i a small negative value considering the observed systematic trend. The other parameters, namely, $R_{\rm hfs}$ and dR, might be freely varied in a fit or fixed at a selected value.

Similarly, we have to consider the magnitude of the effective spin-spin interaction. We observed, introducing only the direct spin-spin interaction, that the splittings for each component (G_1, G_2) with its manifold $F = G_1 + G_2$ would become too large compared to observations. Adding the second-order spin-orbit contribution will reduce this effect and we describe this in a functional form, which was successful in several other cases already (see e.g., [4])

$$\lambda(R) = -\frac{3}{4\alpha^2}\left(\frac{1}{R^3} + a_1^{\rm SO}\exp\left(-b_1^{\rm SO}R\right) + a_2^{\rm SO}\exp\left(-b_2^{\rm SO}R\right)\right), \tag{10}$$

where $\alpha = 137.036$ is the fine-structure constant and the other parameters are degrees of freedom for the fit. The first term is the direct spin-spin interaction and the two others model the spin-orbit contribution. If R is introduced with atomic units in the expression (10), then λ will also result in atomic energies.

By these simple functions for hfs and effective spin-spin interactions the observations could be fitted with normalized standard deviation slightly below one. Figure 5 shows the obtained quality by the example $v_a = 5$ and also the quantum number assignment. The good agreement between the theoretical calculations is visualized in the figure by the vertical

TABLE II. Derived molecular parameters from the fit of the hyperfine pattern of all observed vibrational levels of state $a\,^3\Sigma^+$.

Parameter	Value	Unit
b_{Na}	–0.0417	dimensionless
b_{K}	−0.0634	dimensionless
R_{hfs}	9.70986	bohrs
dR	3.6545	bohrs
a_1^{SO}	−0.07989	bohr^{-3}
a_2^{SO}	−0.00039	bohr^{-3}
b_1^{SO}	0.60	bohr^{-1}
b_2^{SO}	0.10	bohr^{-1}

bars below the experimental spectra. Each bar represents the corresponding calculated hyperfine component. By the dipole selection rules the only possible transitions from the excited mixed state (mainly $B\,^1\Pi/c\,^3\Sigma^+$) $J = 6$, $F_1 = 15/2$, and $F' = 6,7,8,9$ to the state $a\,^3\Sigma^+$ have total angular momenta $F = 10,9,8,7,6,5$ for the lower state. Transitions to existing final levels $F = 4,3,2$ do not appear. The partly unresolved splitting within a component (G_1, G_2) leads to asymmetric line profiles as can be seen in Fig. 5. The model describes with the same precision the deeply bound states ($v_a = 2,3$) up to the asymptotic region ($v_a = 17,18$), where the energy levels are determined by almost pure atomic parameters. The resulting molecular parameters are given in Table II.

During the refinement of the model we introduced also the molecular quadrupole hyperfine interaction, the atomic counterpart of which does not exist for the atomic ground state because the total electronic angular momentum is only $1/2$ for each atom. The deviations between observations and calculations slightly decreased on average, but the resulting quadrupole coupling constants for Na or K were much too large to believe that we really derived a contribution of this interaction. Therefore, it was neglected in the final result.

From the measurements of the pump and dump frequencies in the Λ scheme we derive the energy difference of the two lower levels. If we always apply the same pump transition we obtain by the differences the rovibrational energy ladder with respect to a fixed lowest level, i.e., one singlet rovibrational level. Table III presents these results for the singlet level $v_X = 0, J_X = 6$. In the first two columns the quantum numbers v_a and N_a of the level of state $a\,^3\Sigma^+$ are given to which the laser dumps. In addition, ν_{dump} is the dump frequency and ν_Δ is the frequency difference $\nu_\Delta = \nu_{\mathrm{pump}} - \nu_{\mathrm{dump}}$ and gives the energy of the selected hyperfine component $(G_1 = 1/2, G_2 = 2)$ of the state $a\,^3\Sigma^+$ with respect to the level $J_X = 6$, $v_X = 0$ of the ground state $X\,^1\Sigma^+$ with negligible hyperfine splitting. The averaged pump frequency was 17 451.9549 cm^{-1}. The exact readings for ν_{pump} for each measurement are not given in the table; they can easily be calculated from the formula above. We achieved an absolute uncertainty of 0.0015 cm^{-1}. The energy difference $\nu_{\Delta 0}$ is obtained from ν_Δ by subtracting the hyperfine energy calculated from the final model derived above. We incorporated this result in the potential fit to improve the triplet potential, which up to now was based on the heat-pipe experiments and Fourier-transform spectroscopy

TABLE III. Transition frequencies and energy differences for ^{23}Na^{39}K. Here ν_{dump} is the measured dump frequency from the intermediate level to the same hyperfine component of various rovibrational levels ($v_a = 2$–17 for $N_a = 8$ and $v_a = 3$–17 for $N_a = 6$). The intermediate level was pumped by the transition $[F_1 = 15/2, {}^RQ(6)(8/30\text{–}0)]$ with an averaged pump frequency of 17 451.9549 cm^{-1}. Further, $\nu_\Delta = \nu_{\mathrm{pump}} - \nu_{\mathrm{dump}}$ gives the pump-dump frequency difference and $\nu_{\Delta 0}$ is the position of the pure rotational level with respect to $v_X = 0, J_X = 6$, correcting ν_Δ for the hyperfine and spin-spin contribution derived with the model obtained from the hyperfine analysis. The absolute uncertainty is 0.0015 cm^{-1} and the statistical one is 0.001 cm^{-1}.

v_a	N_a	ν_d (cm^{-1})	ν_Δ (cm^{-1})	$\nu_{\Delta 0}$ (cm^{-1})
3	6	12377.7335	5074.2203	5074.2601
4	6	12359.7967	5092.1583	5092.1982
5	6	12343.1383	5108.8163	5108.8562
9	6	12289.5499	5162.4054	5162.4454
13	6	12257.2723	5194.6826	5194.7227
16	6	12246.5103	5205.4453	5205.4854
17	6	12245.0462	5206.9097	5206.9496
2	8	12395.8526	5056.1012	5056.1409
3	8	12376.6870	5075.2668	5075.3066
4	8	12358.7901	5093.1650	5093.2048
5	8	12342.1741	5109.7808	5109.8207
9	8	12288.7685	5163.1852	5163.2249
13	8	12256.7260	5195.2289	5195.2691
16	8	12246.1873	5205.7670	5205.8071
17	8	12244.8099	5207.1444	5207.1843

with a resolution of 0.03 cm^{-1} and an absolute uncertainty of 0.005 cm^{-1} [22] (see also [39]).

The hyperfine components with $G_1 = 1/2,5/2$ result only when the sodium nuclear spin $i_{\mathrm{Na}} = 3/2$ couples with electron spin $S = 1$, but $G_1 = 3/2$ appears for both values of the total electron spin $S = 0$ and 1. Thus the triplet-singlet mixing is expected to show up most clearly in this subgroup of the hyperfine pattern. Figure 4 demonstrates a significant hfs change in the center part for the last two vibrational levels, namely, for $v_a = 17$ and 18, where strong singlet-triplet mixing takes place for the weakly bound molecular states. This effect is correctly described with our approach and results in a precise knowledge of the singlet-triplet spacing between the last vibrational levels of both electronic states, specifically for a rotational state $N = 6$, $v_X = 72$, and $v_a = 18$.

VI. DISCUSSION

Our observations significantly improve the former investigation of the state $a\,^3\Sigma^+$ by Ishikawa [25]. Their obtained resolution was sufficient for showing the G_2 components of the groups for $G_1 = 1/2,5/2$, but the group $G_1 = 3/2$ was observed as an unresolved feature. We achieved high-resolution spectra where all the G_2 components are completely resolved, partially revealing also the rotational splitting $(\vec{G}_2 + \vec{N} = \vec{F})$ for the groups $G_1 = 3/2,5/2$. We reached the last vibrational levels $v_a = 18$ for the rotational states with $N = 6$ of ^{23}Na^{39}K, which was not observed before. Starting from the tightly

bound states ($v_a = 2,3$) up to the last vibrational levels, the vibrational and thus the R dependence of the hfs is clearly visible. Its magnitude is a few percent of the pure atomic Fermi contact interaction and it is always negative, thus lowering the electron density at each nucleus. This is consistent with the chemical intuition that by molecular binding the electron density is shifted to the region between the two nuclei. The contributions for the R dependence are different for Na and K. Whether this difference is significant is not yet conclusive, because our derived values are notably correlated for both nuclei and also with the derived spin-orbit contribution in $\lambda(R)$ [Eq. (10)]. This latter function is mainly determined by the observed splitting for the (G_1, G_2) subgroups. If one would take only the pure spin-spin interaction given as the $1/R^3$ function in Eq. (10) into account, the calculated spectra would show large splittings in these subgroups, which would be inconsistent with observations.

The rovibrational energies of the triplet state levels derived from frequency measurements of the Λ scheme were applied to improving the $a\,^3\Sigma^+$ potential curve reported from the heat-pipe study [22]. Due to the convolution of the apparatus profile of the Fourier-transform spectrometer (FTS) (resolution of 0.02–0.05 cm^{-1}) and the Doppler profile (width 0.03 cm^{-1}) of the hot ensemble in the heat pipe, the hfs remained unresolved and the transitions to the triplet state were observed as asymmetric lines with a full width at half maximum of 0.075 cm^{-1}. The peaks of these lines were reported for the FTS results. The direct comparison with the beam data shows that the energies from the heat pipe are systemically shifted by about 0.02–0.03 cm^{-1} for the ladder with $N = 6$ and 8. This is more than the uncertainty of 0.005 cm^{-1} given in [22]. Accordingly, we enlarged the uncertainty of the FTS data for the evaluation process.

Finally, we also incorporated in our evaluation the data of the Feshbach resonances reported by Park *et al.* [6]. Especially the p resonances contribute to the knowledge of the function of $\lambda(R)$. All fit results shown in the tables include all known experimental data from spectroscopy (see [22] and the present work) and cold collisions [6]. The subset of the Feshbach resonances taken from the total fit shows a normalized standard deviation of $\sigma = 1.8$ when taking the uncertainties reported by [40] fully into account. The deviations of this subset of data are slightly larger compared to a separate fit of Feshbach data alone, giving $\sigma = 1.5$. Both results are statistically not completely convincing and further investigations are required to check the experimental results and seek further extensions of the theoretical model. The difference in the two fits could result from the fact that the Feshbach data give information of the triplet-singlet mixing of the high vibrational levels for $N = 0$ and 1 (second to last $v_X = 73$ and last $v_a = 19$), whereas the spectroscopy by the present work studied this coupling for the last vibrational levels for $N = 6$ (third to last $v_X = 72$ and second to last $v_a = 18$). If this idea is essential for the remaining inconsistency, the long-range function in the potential approach is not yet satisfactorily described. Nevertheless, the present modeling of the Feshbach observation is significantly improved compared to the case in [6] and this fact allows us to give better values than in [22] for the scattering length of NaK, which is important for future cold collision studies of Na + K. Calculated values are shown in Table IV. The s-wave resonances observed in [6] show only small contributions of the singlet state, thus the scattering length of the singlet is more strongly determined by the singlet-triplet mixing observed by the present spectroscopy as shown in Fig. 4 and these two effects lead to significantly different estimates of the uncertainties of the calculated scattering lengths in Table IV. The values agree with earlier calculations in [22] within the significantly larger errors reported there.

TABLE IV. Derived scattering length for the different isotopes of Na + K collisions.

Isotope	Singlet	Triplet	Unit
^{23}Na + ^{39}K	324(10)	–83.9(10)	bohrs
^{23}Na + ^{40}K	66.4(10)	–823(5)	bohrs
^{23}Na + ^{41}K	2.88(40)	267.2(10)	bohrs

An important motivation of the present spectroscopic study was the identification of efficient routes for production of ultracold NaK starting with ultracold atomic ensembles and Feshbach molecules. The Λ scheme applied here used the rotational angular momentum $N = 6$, which is certainly not adequate for ultracold collisions and resulting ultracold molecules. However, according to the study of Katô and co-workers [23,41] and also our present beam study recording the full band head of $B\,^1\Pi/c\,^3\Sigma^+$–$X\,^1\Sigma^+(8/30–0)$, the perturbation is significant even for the rotational level $J = 1$ with negative parity as required for a starting level of an ultracold atom pair with $N = 0$ and thus positive parity. In Fig. 6 we give the recording of the $R(0)$ transitions leading to the two mixed

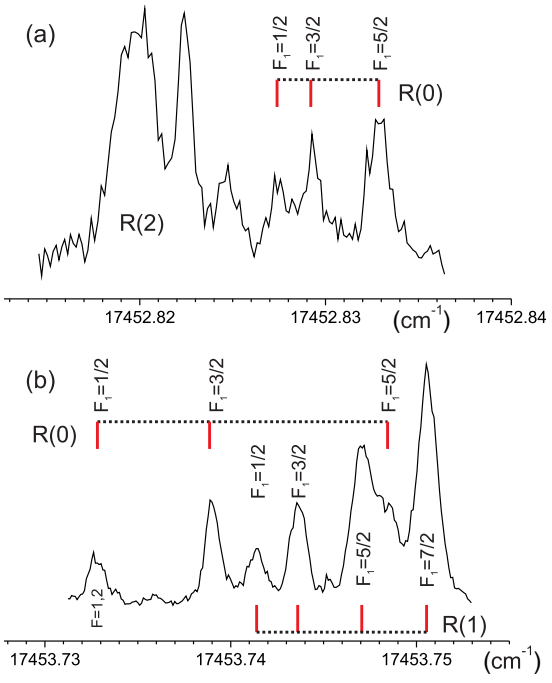

FIG. 6. (Color online) Observed low J transitions in the 8/30–0 band of $B\,^1\Pi/c\,^3\Sigma^+$-$X\,^1\Sigma^+$ for ^{23}Na^{39}K in the molecular beam with dominant amplitude of (a) the $B\,^1\Pi$ state and (b) the $c\,^3\Sigma^+$ state.

states. Figure 6(a) shows the transition to the intermediate level with dominant $B\,^1\Pi$ amplitude and Fig. 6(b) with dominant $c\,^3\Sigma^+$ amplitude. Adjacent $R(1)$ or $R(2)$ transitions are contained in the figure. We confirmed the assignment by observing the $P(2)$ transition corresponding to the $R(0)$ lines shifted in frequency according to the well-known rotational energy of the ground state $X\,^1\Sigma^+$ and presenting the same hfs splitting as the $R(0)$ transition. The signal-to-noise ratio is different in both recordings because of different experimental conditions by the time of observation. The perturbation results in significant amplitudes for $B\,^1\Pi$ and $c\,^3\Sigma^+$ as required for an efficient Λ scheme with an initial Feshbach level. The individual hyperfine transitions can be read off from the figure by the detailed scale of the frequency axis, for the center of the structure $B\,^1\Pi$ $(v = 8)/c\,^3\Sigma^+$ $(v = 30)$ the values of the two perturbed energies are 17514.71 and 17515.61 cm^-1 with respect to the potential minimum of $X\,^1\Sigma^+$ and results to the two possible $R(0)\,v = (8/30 - 0)$ transitions 17452.83 and 17453.74 cm^{-1}.

For further predictions of efficient production paths, especially for the Bose-Fermi isotope $^{23}Na^{40}K$, using the resonance case for the reversed Λ scheme in contrast to the broadband approach presented in [20], we refined the theoretical model given by Ferber *et al.* [24] for the molecular states correlating to the atomic asymptote $Na(3s) + K(4p)$ as shown in Fig. 1. We added all the $\Omega = 0$ states and completed for the $\Omega = 1$ states the coupling between $B\,^1\Pi$ and $b\,^3\Pi$. Using potential functions (or Dunham parameters for their construction with the conventional Rydberg-Klein-Rees method) reported by different groups [23,24,42], we were able, by small tunings of the potentials (less than 1 cm^{-1}), to reproduce within about ± 0.1 cm^{-1} primary observations in a significant energy range, namely, $v = 0$–13 of $B\,^1\Pi$ checking low J data obtained from the supplement to [24] or our own measurements [43] and the perturbation of the system $A\,^1\Sigma^+$–$b\,^3\Pi$ taking data from Sun and Huennekens [44]. We not only reproduced the energies but also found the significant perturbations at the reported places. After this success on $^{23}Na^{39}K$ we are confident that predictions for $^{23}Na^{40}K$ will lead to an accuracy that is sufficient to plan reliably production schemes also for this isotope pair. One example being fairly similar to the above-mentioned case for $^{23}Na^{39}K$ will be for $^{23}Na^{40}K$ and $J = 1$ with negative parity: $B\,^1\Pi$ $(v = 4)$–$c\,^3\Sigma^+$ $(v = 25)$ with the two perturbed energies 17 288.8 and 17 289.2 cm^{-1} with respect to the potential minimum of $X\,^1\Sigma^+$ resulting in two $R(0)$ $v = 4/25$–0 transitions at 17 227.2 and 17 227.6 cm^{-1}.

We cannot check this prediction in our beam apparatus because of the too low natural abundance of ^{40}K and unaffordable enriched samples. To predict other possible cases would be straightforward if required by experimental groups. An evaluation of the full system to improve further the modeling of the electronic system belonging to the asymptote $Na(3s) + K(4p)$ performed partly by others (see, e.g., [24,44]) is left for future work.

ACKNOWLEDGMENTS

The work was carried out with support from the Centre of Excellence QUEST at the Leibniz University. We would like to thank the members of the mechanical workshop of our institute for the quick response every time when we needed their help immediately. E.T. gratefully acknowledges support from the Minister of Science and Culture of Lower Saxony, through Volkswagenstiftung Germany, by providing a Niedersachsenprofessur.

[1] J. Stuhler, A. Griesmaier, T. Koch, M. Fattori, T. Pfau, S. Giovanazzi, P. Pedri, and L. Santos, Phys. Rev. Lett. **95**, 150406 (2005).
[2] U. Gaubatz, P. Rudecki, S. Schiemann, and K. Bergmann, J. Chem. Phys. **92**, 5363 (1990).
[3] K. K. Ni, S. Ospelkaus, M. H. G. de Miranda, A. Pe'er, B. Neyenhuis, J. J. Zirbel, S. Kotochigova, P. S. Julienne, D. S. Jin, and J. Ye, Science **322**, 231 (2008).
[4] M. P. Köppinger, D. J. McCarron, D. L. Jenkin, P. K. Molony, H.-W. Cho, S. L. Cornish, C. R. Le Sueur, C. L. Blackley, and J. M. Hutson, Phys. Rev. A **89**, 033604 (2014).
[5] M. Repp, R. Pires, J. Ulmanis, R. Heck, E. D. Kuhnle, M. Weidemuller, and E. Tiemann, Phys. Rev. A **87**, 010701 (2013).
[6] J. W. Park, C. H. Wu, I. Santiago, T. G. Tiecke, S. Will, P. Ahmadi, and M. W. Zwierlein, Phys. Rev. A **85**, 051602(R) (2012).
[7] C. H. Wu, J. W. Park, P. Ahmadi, S. Will, and M. W. Zwierlein, Phys. Rev. Lett. **109**, 085301 (2012).
[8] J. Deiglmayr, A. Grochola, M. Repp, K. Mörtlbauer, C. Glück, J. Lange, O. Dulieu, R. Wester, and M. Weidemüller, Phys. Rev. Lett. **101**, 133004 (2008).
[9] C. Gabbanini and O. Dulieu, Phys. Chem. Chem. Phys. **13**, 18905 (2011).
[10] C. D. Bruzewicz, M. Gustavsson, T. Shimasaki, and D. de Mille, New J. Phys. **16**, 023018 (2014).
[11] T. Shimasaki, M. Bellos, C. D. Bruzewicz, Z. Lasner, and D. de Mille, arXiv:1407.7512.
[12] P. Zabawa, A. Wakim, M. Haruza, and N. P. Bigelow, Phys. Rev. A **84**, 061401(R) (2011).
[13] J. Banerjee, D. Rahmlow, R. Carollo, M. Bellos, E. E. Eyler, P. L. Gould, and W. C. Stwalley, Phys. Rev. A **86**, 053428 (2012).
[14] M. Aymar and O. Dulieu, J. Chem. Phys. **122**, 204302 (2005).
[15] J. Deiglmayr, A. Grochola, M. Repp, O. Dulieu, R. Wester, and M. Weidemüller, Phys. Rev. A **82**, 032503 (2010).
[16] R. F. Wormsbecher, M. M. Hessel, and F. J. Lovas, J. Chem. Phys. **74**, 6983 (1981).
[17] T. Takekoshi, L. Reichsöllner, A. Schindewolf, J. M. Hutson, C. R. Le Sueur, O. Dulieu, F. Ferlaino, R. Grimm, and H.-C. Nägerl, Phys. Rev. Lett. **113**, 205301 (2014).
[18] P. S. Zuchowski and J. M. Hutson, Phys. Rev. A **81**, 060703 (2010).

[19] S. Ospelkaus, K. K. Ni, D. Wang, M. H. G. de Miranda, B. Neyenhuis, G. Quéménér, P. S. Julienne, J. L. Bohn, D. S. Jin, and J. Ye, Science **327**, 853 (2010).
[20] T. A. Schulze, I. I. Temelkov, M. W. Gempel, T. Hartmann, H. Knöckel, S. Ospelkaus, and E. Tiemann, Phys. Rev. A **88**, 023401 (2013).
[21] I. Russier-Antoine, A. J. Ross, M. Aubert-Frécon, F. Martin, and P. Crozet, J. Phys. B **33**, 2753 (2000).
[22] A. Gerdes, M. Hobein, H. Knöckel, and E. Tiemann, Eur. Phys. J. D **49**, 67 (2008).
[23] H. Katô, M. Sakano, N. Yoshie, M. Baba, and K. Ishikawa, J. Chem. Phys. **93**, 2228 (1990).
[24] R. Ferber, E. A. Pazyuk, A. V. Stolyarov, A. Zaitsevskii, P. Kowalczyk, H. Chen, H. Wang, and W. C. Stwalley, J. Chem. Phys. **112**, 5740 (2000).
[25] K. Ishikawa, J. Chem. Phys. **98**, 1916 (1993).
[26] K. Ishikawa, N. Mukai, and M. Tanimura, J. Chem. Phys. **101**, 876 (1994).
[27] S. Knoop, T. Schuster, R. Scelle, A. Trautmann, J. Appmeier, M. K. Oberthaler, E. Tiesinga, and E. Tiemann, Phys. Rev. A **83**, 042704 (2011).
[28] A. Gerdes, O. Dulieu, H. Knöckel, and E. Tiemann, Eur. Phys. J. D **65**, 105 (2011).
[29] S. Falke, Ph.D. thesis, University of Hannover, 2007.
[30] A. Stein, Diploma thesis, University of Hannover, 2006.
[31] S. Falke, E. Tiemann, C. Lisdat, H. Schnatz, and G. Grosche, Phys. Rev. A **74**, 032503 (2006).
[32] J. Derouard, H. Debontride, T. D. Nguyen, and N. Sadeghi, J. Chem. Phys. **90**, 5936 (1989).
[33] S. Falke, H. Knöckel, J. Friebe, M. Riedmann, E. Tiemann, and C. Lisdat, Phys. Rev. A **78**, 012503 (2008).
[34] G. Audi, A. H. Wapstra, and C. Thibault, Nucl. Phys. A **729**, 337 (2003).
[35] E. Arimondo, M. Inguscio, and P. Violino, Rev. Mod. Phys. **49**, 31 (1977).
[36] A. Derevianko, J. F. Babb, and A. Dalgarno, Phys. Rev. A **63**, 052704 (2001).
[37] S. G. Porsev and A. Derevianko, J. Chem. Phys. **119**, 844 (2003).
[38] B. M. Smirnov and B. I. Chibisov, JETP **21**, 624 (1965).
[39] See Supplemental Material at http://link.aps.org/supplemental/10.1103/PhysRevA.91.032512 for the potential parameters according to the definitions in Eqs. (5), (6), and (7).
[40] M. W. Zwierlein (private communication).
[41] K. Ishikawa, T. Kumauchi, M. Baba, and H. Katô, J. Chem. Phys. **96**, 6423 (1992).
[42] A. Ross *et al.*, J. Mol. Spectrosc. **127**, 546 (1988).
[43] A. Gerdes, Ph.D. thesis, University of Hannover, 2010.
[44] H. Sun and J. Huennekens, J. Chem. Phys. **97**, 4714 (1992).